Determination of the Yield Properties of Thin Films Using Enhanced Coherent Gradient Sensing

by R. P. Singh and A. J. Rosakis

ABSTRACT—This paper describes coherent gradient sensing (CGS) as an optical, full-field, real-time, nonintrusive, noncontact technique for measurement of curvature and curvature changes in single-layered and multilayered thin films deposited on substrates. The sensitivity of the basic CGS technique is enhanced using optical fringe multiplication to map curvature in very flat specimens ($\kappa \leq 0.001$ m^{-1}). Subsequently, this curvature measurement technique is applied to the determination of the yield properties of thin films subjected to cyclic thermomechanical loading.

KEY WORDS—Thin films, curvature, stress, coherent gradient sensing

Introduction

As the electronics industry pushes for smaller and smaller dimensions of metal interconnections and for more complex multilayered structures, the mechanical properties and stresses of thin films used for these interconnections will be crucial to the lifetimes of ultra large scale integrated circuits.[1,2] However, the difficulty in measuring the mechanical properties and stresses of interconnections increases as their size decreases.[3] Currently, the major concern for interconnection materials is the presence of residual stresses from the fabrication process and additional stresses resulting from thermal cycling.[4,5]

Typically, integrated circuit metallization consists of many layers deposited onto a silicon substrate, very often at elevated temperatures. The layers exhibit different mechanical, physical and thermal properties, leading to high stresses in interconnection structures. These stresses cause stress-induced voiding,[6–18] are directly related to electromigration[19–25] and may cause cracking of the substrate.[3] All of the preceding are leading failure mechanisms in integrated circuits. An understanding of stresses and their distribution and origins is a crucial step in improving the reliability of integrated circuits.

Currently used experimental techniques for measuring stresses are based either on direct measurements of strains in the films using X-ray diffraction[26,27] or on the measurements of substrate curvature or deflection.[28] Curvature and curvature change measurements are typically related to the stress state in the layered structures by means of theoretical analyses based either on approximate plate theories[29,30] or, more recently, on exact continuum mechanics formulation.[31,32]

The X-ray diffraction technique typically employed for polycrystalline materials involves measuring d-spacings of a single reflection for several orientations of the sample.[26] This procedure determines strains along different directions of the sample. The technique is nondestructive, does not require special sample configurations and permits measurements of all the components of stress in the film. However, it is limited to crystalline materials (e.g., stresses in passivation layers cannot be measured) and is difficult to use in situ during film growth. Moreover, the method is strictly pointwise; that is, full-field, instantaneous measurement of stresses is not possible.

Curvature measurements in thin films can also be made by high-resolution X-ray diffraction using a modified X-ray rocking curve setup.[27] With a translation stage added to the conventional rocking curve system, the shift in the substrate Bragg peak can be measured at different lateral positions on a film deposited on a single crystal substrate. The average principal stresses can then be found from the peak shift. However, this technique requires that calibration and curvatures be measured only *relative* to the reference calibration specimen. The technique cannot be easily adapted for in situ measurements because motion of the sample is required, and because the method is strictly pointwise, full-field instantaneous curvature measurements are not possible.

Laser scanning is the most commonly used technique for determining stresses in thin films by measuring curvature changes of the substrate.[28] This technique is very sensitive and is capable of detecting up to 10^4 m radius of curvature. However, the laser-scanning technique provides pointwise information and could potentially miss localized anomalies in specimen curvature. Even if complete curvature maps were generated by scanning, these scans would involve finite time and may not be adequate for time varying, nonuniform surface curvature fields (e.g., a growing delamination due to thermal cycling).

Techniques based on optical interferometry offer much promise as a means for real-time, remote, nonintrusive, full-field measurements of curvature and curvature changes. However, standard interferometric techniques, such as Twyman-Green interferometry,[33,34] are sensitive to rigid-body rotation and displacement of the specimen surface and, thus, are very vibration sensitive. Moreover, because these interferometric techniques measure surface topography, two successive differentiations of the experimental data are required to obtain curvature.

R. P. Singh (SEM Member) is an Assistant Professor, Department of Mechanical Engineering, State University of New York, Stony Brook, NY 11794. A. J. Rosakis (SEM Member) is a Professor, Graduate Aeronautical Laboratories, California Institute of Technology, Pasadena, CA 91125.

Original manuscript submitted: October 2, 2000.
Final manuscript received: May 10, 2001.

Recently, Rosakis *et al.*[35,36] demonstrated coherent gradient sensing (CGS) as a full-field, optical technique for the instantaneous measurement of curvature and curvature changes in various thin film structures. This technique is insensitive to rigid-body rotation and translation of the curved specimen. Also, only one differentiation of the experimental data is required to obtain the curvature components.

In this paper, the sensitivity of the CGS technique is enhanced using optical fringe multiplication. This enhanced CGS technique is then applied successfully to characterize yield properties of thin films.

Curvature Measurement Using CGS

Figure 1 shows a schematic of the CGS setup in reflection. A coherent, collimated laser beam is directed to the specularly reflecting specimen surface by means of a beam splitter. The reflected beam from the specimen then passes through the beam splitter and is incident upon a pair of identical high-density (40 lines/mm) Ronchi gratings, G_1 and G_2, separated by a distance Δ. The diffracted orders from the two gratings are spatially filtered using a filtering lens to form distinct diffraction spots on the filter plane. An aperture placed in this plane serves to filter out the diffraction order of interest, which is then imaged onto the film plane. A photograph of the actual experimental setup is shown in Figure 2.

The interpretation and working principle of CGS was presented by Lee *et al.*[37] using Fourier optics and by Rosakis *et al.*[35] using simple geometric optics. For the case of wave front "shearing" in either the x_1- or the x_2-direction, the CGS interferograms can be interpreted as

$$\frac{\partial S(x_1, x_2)}{\partial x_a} = \frac{n^{(a)} p}{\Delta} \quad n^{(a)} = 0, \pm 1, \pm 2, \ldots , \qquad (1)$$

where $S(x_1, x_2)$ represents the optical wave front reflected from the specimen surface, $n^{(\alpha)}$ are the fringes observed for shearing along the x_α-direction, p is the grating pitch, Δ is the grating separation and $\alpha \in \{1, 2\}$. Equations (1) govern the formation of interferograms using the technique of CGS.

For a curved surface, the optical wave front may be interpreted in terms of the topography of the surface. Consider a specularly reflective specimen whose curved surface (i.e., the reflector) is given as $x_3 = f(x_1, x_2)$. Then, it can be shown that[35,37]

$$S(x_1, x_2) = f(x_1, x_2) \left(\frac{2}{1 - f_{,1}^2 - f_{,2}^2} \right). \qquad (2)$$

Assuming and substituting eq (2) in eqs (1), we get

$$\frac{\partial f(x_1, x_2)}{\partial x_a} \approx \frac{n^{(a)} p}{2\Delta} \quad n^{(a)} = 0, \pm 1, \pm 2, \ldots , \qquad (3)$$

where $\alpha \in \{1, 2\}$. Equations (3) are the basic governing equations that relate CGS fringe contours to in-plane gradients of the specimen surface $x_3 = f(x_1, x_2)$.

For a shallow surface given by $x_3 = f(x_1, x_2)$, the components of the curvature tensor are expressed as[35]

$$\kappa_{\alpha\beta} \approx f_{,\alpha\beta} \quad \alpha, \beta \in \{1, 2\}, \qquad (4)$$

where $\kappa_{\alpha\beta}$ is the symmetric curvature tensor whose components κ_{11} and κ_{22} are the "normal curvatures" and κ_{12} $(= \kappa_{21})$ is the "twist." The principal values of $\kappa_{\alpha\beta}$ are the principal curvatures. Substituting eqs (4) into eqs (3), we get the basic equations that relate CGS fringes to specimen curvature,

$$\kappa_{\alpha\beta}(x_1, x_2) \approx \frac{\partial^2 f(x_1, x_2)}{\partial x_a \partial x_\beta} \approx \frac{p}{2\Delta} \left(\frac{\partial n^{(a)}(x_1, x_2)}{\partial x_\beta} \right) \qquad (5)$$

$$n^{(a)} = 0, \pm 1, \pm 2, \ldots ,$$

where $\alpha \in \{1, 2\}$. Equations (5) are the principal governing equations for determining curvature tensor fields, $\kappa_{\alpha\beta}(x_1, x_2)(\alpha, \beta \in \{1, 2\})$, from CGS interferograms. In this manner, CGS interferograms provide a full-field technique for determining the instantaneous value of the specimen curvature tensor at any point $(x1_{,}x_2)$.

The CGS technique has been employed to determine curvature tensor components in various thin film and microelectronic specimens.[35] The specimen was manufactured by the Massachusetts Institute of Technology's Lincoln Laboratories and comprised multilayered thin films deposited on a

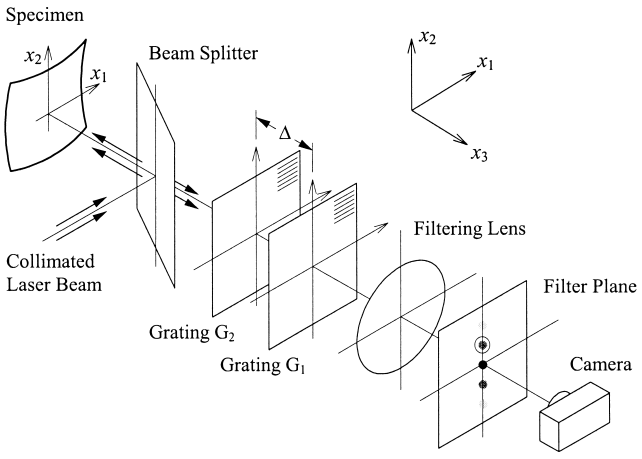

Fig. 1—Schematic of the coherent gradient sensing setup in reflection mode

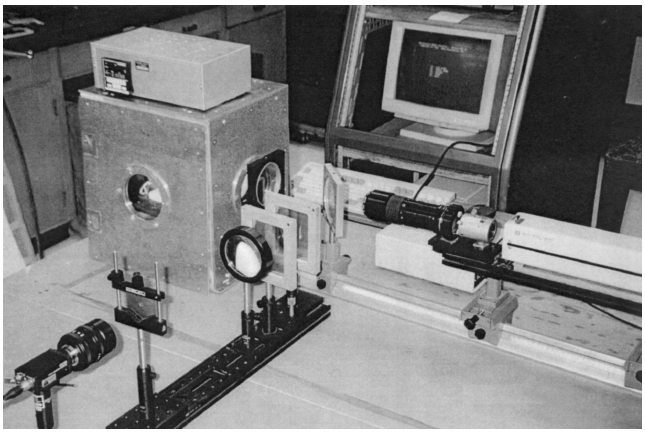

Fig. 2—Photograph showing the coherent gradient sensing interferometer used to measure curvature. The specimen is placed inside a box furnace, which can provide thermal cycling

single crystal silicon wafer. The layered structures of the two specimens (multilayer A and multilayer B) are tabulated in Table 1. CGS interferograms obtained from multilayer A are shown in Figure 3. Separate interferograms were obtained for wave front shearing in two orthogonal directions. These interferograms were then digitized and numerically differentiated to determine components of the curvature tensor field as per eq (5). These curvature components, κ_{11}, κ_{22} and κ_{12}, are plotted in Figure 4. The specimen exhibited fairly uniform curvature toward the center despite considerable variation toward some of the edges. Also, there was about an 18-percent difference in the normal curvatures, κ_{11} and κ_{22}, measured along the x_1 and x_2 directions. This could be due to inherent material anisotropy of the silicon substrate and directional structural variation in the thin film coatings associated with the fabrication process. The twist curvature, κ_{12}, was considerably smaller in magnitude than the normal curvatures, κ_{11} and κ_{22}, and had a maximum value near the specimen edge.

Average curvature was obtained using high-resolution X-ray diffraction for the sake of comparison with the CGS data. Details of these measurements are given in Rosakis *et al.*[35] Because high-resolution X-ray diffraction measures curvature only in an averaged sense, the CGS data were also averaged to facilitate a direct comparison of curvatures obtained using the two techniques. Averaging of the curvature fields obtained using CGS was done in the center of the specimen because this is the area where X-ray diffraction measures average curvature. Table 2 lists the averaged curvature measurements made using the two techniques for both multilayer A and multilayer B specimens. As given in the table, the agreement between the two techniques (for the κ_{22} component) was excellent. Note that direct comparison between the *absolute* curvatures measured by CGS and the *relative* curvatures measured by X-ray diffraction was possible in these cases because the reference specimen used to calibrate the X-ray diffraction technique was "extremely flat" ($\kappa < 0.002$ m^{-1}, as determined by CGS).

CGS was also employed to determine the presence of a surface defect in a chromium-coated silicon wafer (320 nm Cr/324 μm Si). The CGS interferograms obtained for shearing in the two directions are shown in Figure 5. The CGS interferograms were analyzed in accordance with eq (5) to determine components of the curvature tensor field. It is apparent from the normal curvature component, κ_{11}, shown in Figure 6 that there is a highly localized region on the specimen that exhibits very high curvatures relative to the rest of the specimen. This region of high curvature represents a "defect" in the form of a localized nonuniformity of the specimen surface. Whatever the cause of this surface nonuniformity, CGS interferometry is shown to be capable of successfully identifying such surface anomalies because of its full-field nature. Other commonly used curvature measurement methods such as high-resolution X-ray diffraction[26,27] and the laser-scanning technique[28] provide pointwise information and could potentially miss such localized anomalies. Moreover, even if complete curvature maps were to be generated by scanning, these scans would involve finite time and might not be adequate for time varying, nonuniform surface curvature fields (e.g., a growing delamination due to thermal cycling). On the other hand, CGS produces an *instantaneous* full-field map of the entire curvature tensor field.

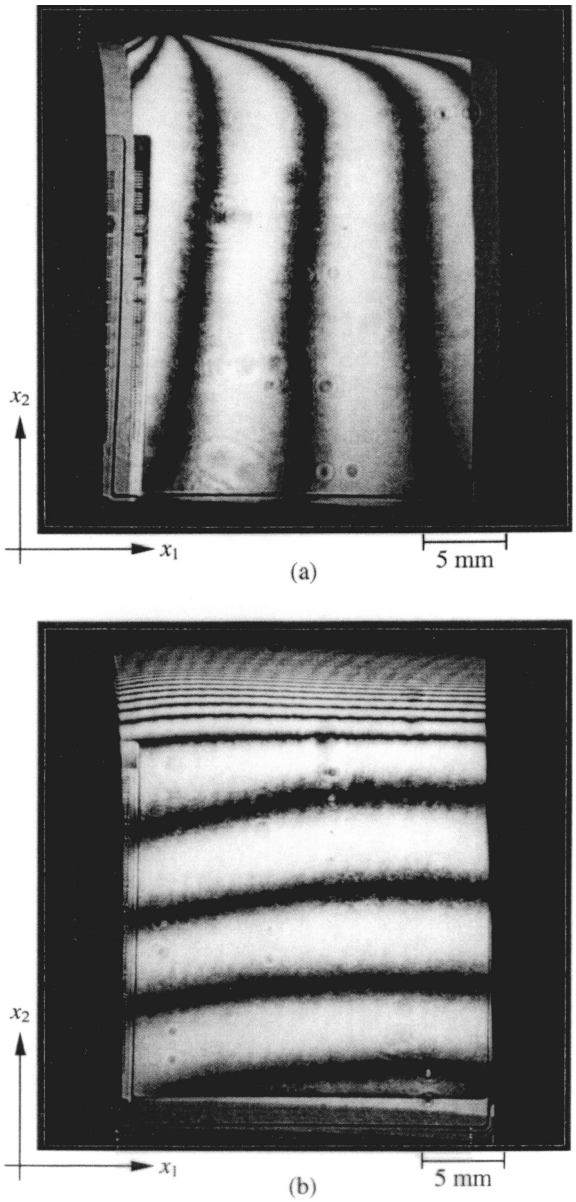

Fig. 3—Coherent gradient sensing interferograms obtained for the multilayer A specimen: (a) shearing along x_1, (b) shearing along x_2

Sensitivity Enhancement for CGS

The minimum curvature that is measurable using CGS is estimated as follows. Consider the limiting case of a highly shallow specimen in which only one fringe order is observed when the shearing distance equals half the specimen width. Then, using a finite difference relation for the phase change in the optical wave front,

$$\delta S = S\left(x_1, x_2 + \frac{d}{2}\right) - S(x_1, x_2) = \lambda, \tag{6}$$

where $d/2$ is half the specimen width and represents the shearing distance and λ is the wavelength of light. Thus, normal curvature is approximated as

$$\kappa_{22} \approx \frac{\partial^2 f}{\partial x^2} \approx \frac{1}{2}\frac{\delta S}{(d/2)^2} = \frac{2\lambda}{d^2}, \tag{7}$$

TABLE 1—LAYERED STRUCTURE OF MULTILAYER A AND MULTILAYER B SPECIMENS OBTAINED USING RUTHERFORD BACK SCATTERING

Layer Constituent	Multilayer A Specimen	Multilayer B Specimen
TiN	—	50 nm
Al-x%Si	500 nm	500 nm
Ti	30 nm	30 nm
TiN	100 nm	100 nm
SiO_2	420 nm	420 nm
Si (substrate)	506 μm	506 μm

TABLE 2—CURVATURES FOR MULTILAYER A AND MULTILAYER B SPECIMEN OBTAINED USING COHERENT GRADIENT SENSING (CGS) (AVERAGED OVER SPECIMEN CENTER) AND HIGH-RESOLUTION X-RAY DIFFRACTION

	Multilayer A Specimen		Multilayer B Specimen	
Curvature	CGS	X-ray Diffraction	CGS	X-ray Diffraction
κ_{11}	0.039 m^{-1}	—	0.024 m^{-1}	—
κ_{22}	0.048 m^{-1}	0.050 m^{-1}	0.039 m^{-1}	0.042 m^{-1}
$\kappa_{12} = \kappa_{21}$	−0.014 m^{-1}	—	−0.004 m^{-1}	—

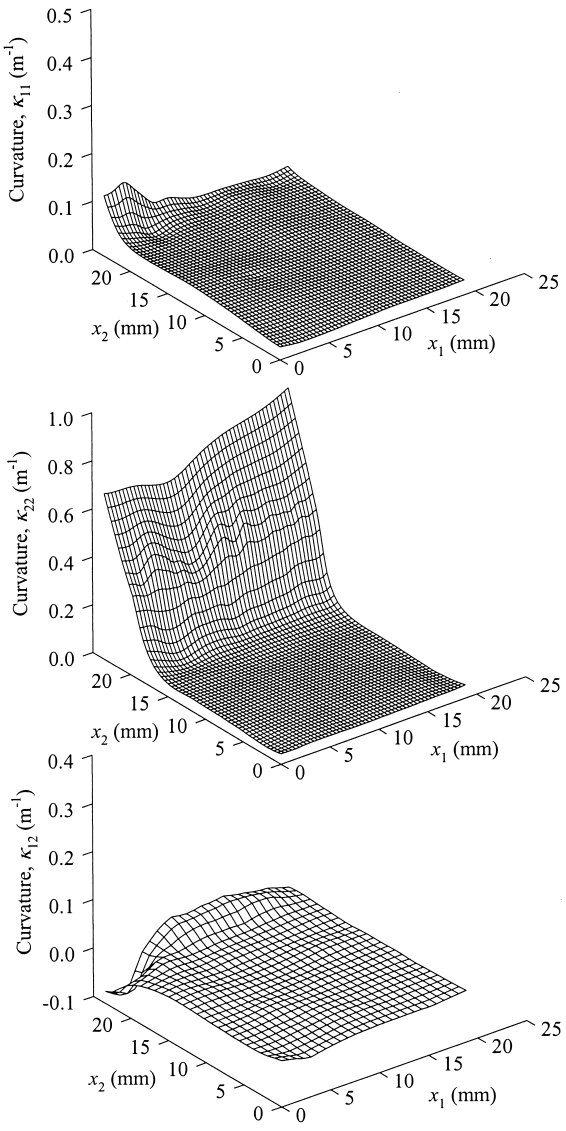

Fig. 4—Curvature tensor components, κ_{11}, κ_{22} and κ_{12}, obtained from coherent gradient sensing interferograms for the multilayer A specimen

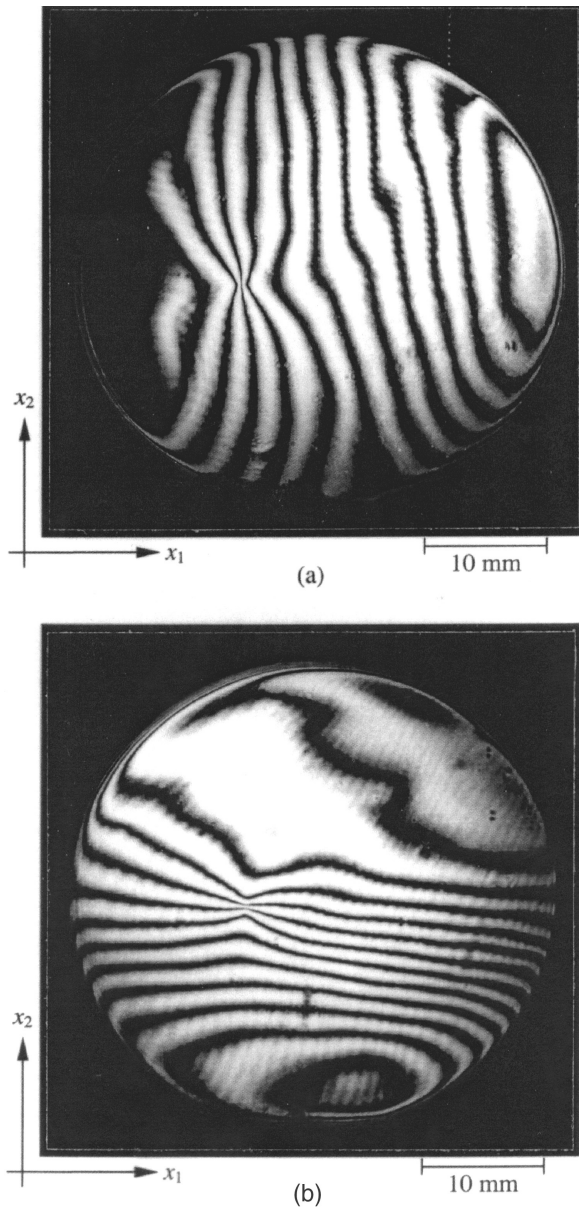

Fig. 5—Coherent gradient sensing interferograms obtained for a thin film chromium-coated silicon wafer with a localized surface defect: (a) shearing along x_1, (b) shearing along x_2

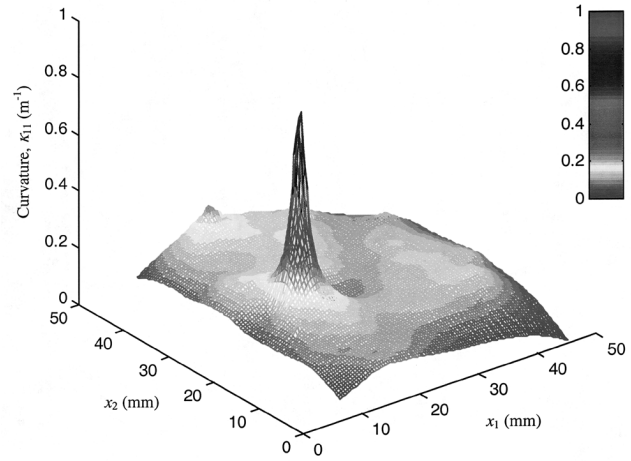

Fig. 6—Normal curvature, κ_{11}, for a thin film chromium-coated silicon wafer with a localized surface defect as obtained from coherent gradient sensing interferograms

where we have used the relation $S(x_1, x_2) \approx 2f(x_1, x_2)$. Therefore, for a typical specimen width of 50 mm and wavelength of light of 632.8 nm, we obtain a limiting minimum value of curvature, $\kappa_{22} \approx 0.001$ m^{-1}, that is, a maximum radius of curvature of 1000 m. Thus, the technique needs to be enhanced for its application to very flat specimens with curvatures $\kappa \leq 0.001$ m^{-1}.

The sensitivity of CGS can be enhanced using an optical fringe multiplication technique. This technique employs a partial mirror placed in front of the reflective specimen, as shown in Figure 7. The partial mirror is placed at a slight inclination angle, α, with respect to the specimen. In this configuration, light is reflected back and forth between the mirror and the specimen, as illustrated in Figure 8. From this figure, it is also clear that each beam of light emerges from the partial mirror at an angle that depends on the number of times the light beam has reflected off the specimen surface. The slight inclination angle α allows the various reflection orders to be separated spatially and has been greatly exaggerated to illustrate the multiple reflection effect.

Each subsequent reflection of the light beam from the curved specimen surface introduces additional change in the optical path length, as compared to reflection from a flat reference surface. The net change in optical path length at point (x_1, x_2) for the Nth-order reflection is given as

$$S(x_1, x_2) \approx 2Nf(x_1, x_2). \tag{8}$$

Substituting eq (8) into eqs (1), we get

$$\frac{\partial f(x_1, x_2)}{\partial x_a} \approx \frac{n^{(a)} p}{2N\Delta} \quad n^{(a)} = 0, \pm 1, \pm 2, \ldots, \tag{9}$$

where $\alpha \in \{1, 2\}$ and N is the fringe multiplication order. Equations (9) are the basic governing equations that relate CGS fringe contours to in-plane gradients of the specimen surface $x_3 = f(x_1, x_2)$ for a given fringe multiplication order. Substituting eqs (9) into eqs (4), we get the equations that relate CGS fringes to specimen curvature for the case of fringe multiplication:

$$\kappa_{\alpha\beta}(x_1, x_2) \approx \frac{\partial^2 f(x_1, x_2)}{\partial x_a \partial x_\beta} \approx \frac{p}{2N\Delta}\left(\frac{\partial n^{(a)}(x_1, x_2)}{\partial x_\beta}\right)$$
$$n^{(a)} = 0, \pm 1, \pm 2, \ldots, \tag{10}$$

where $\alpha \in \{1, 2\}$, $\beta \in \{1, 2\}$ and N is the fringe multiplication order. Thus, the smallest value of curvature that can be measured decreases by a factor equal to the fringe multiplication order.

Typical fringe patterns obtained using fringe multiplication are shown in Figure 9. It is clear from the figure that this technique greatly increases the sensitivity of CGS in measuring curvature tensor fields.

Measurement of Yield Properties of Thin Films on Substrates

The stress-strain behavior and yield properties of thin films play an important role in governing their mechanical response and modes of failure. Moreover, the structure and properties of a material when it is deposited as a thin film are very different from those of the bulk material. In addition, the behavior of a thin film attached to a substrate may be significantly different from that of a freestanding film. Thus, it is necessary to characterize the stress-strain behavior and yield properties of thin films as deposited on substrates.

Standard material testing techniques employed to study the stress-strain behavior of bulk materials are not applicable to the study of thin films. This is primarily due to the much smaller length scales involved in the latter. To study the deformation and mechanical properties of thin films, we need alternative methods for loading the thin film in a controlled manner and measuring the resulting deformation. The loading of thin films deposited on substrates was achieved by varying the temperature of the thin film–substrate system. Usually, there is a significant mismatch in the thermal coefficients of expansion of the thin film and the substrate. This mismatch gives rise to tensile/compressive stresses in both the thin film and the substrate as the temperature is varied. Thermal loading of the thin film–substrate system in this fashion also results in a change in curvature of the system, which can be used to determine specimen deformation.

If we assume perfect adhesion between the thin film and the substrate, the stress in the film is given as[29]

$$\sigma^f_{aa} = \frac{E_s t^2}{6(1 - \nu_s)h}\kappa_{aa} \quad \alpha \in \{1, 2\} \text{ no sum over } \alpha, \tag{11}$$

where $\sigma^f_{\alpha\alpha}$ is the film stress, h is the film thickness, E_s is Young's modulus of the substrate, ν_s is Poisson's ratio of the substrate, t is the substrate thickness and $\kappa_{\alpha\alpha}$ is the normal component of the curvature tensor.

The above relation assumes that the substrate is linear elastic and isotropic and the film thickness is much less than that of the substrate. However, it does not involve any constitutive assumptions for the thin film, which is allowed to be of arbitrary properties. This is a distinct advantage for our investigation, which is aimed at uncovering the virtually unknown stress-strain behavior of the film.

At low values of curvature, the film is expected to remain elastic. In such a case, one is able to relate the elastic film

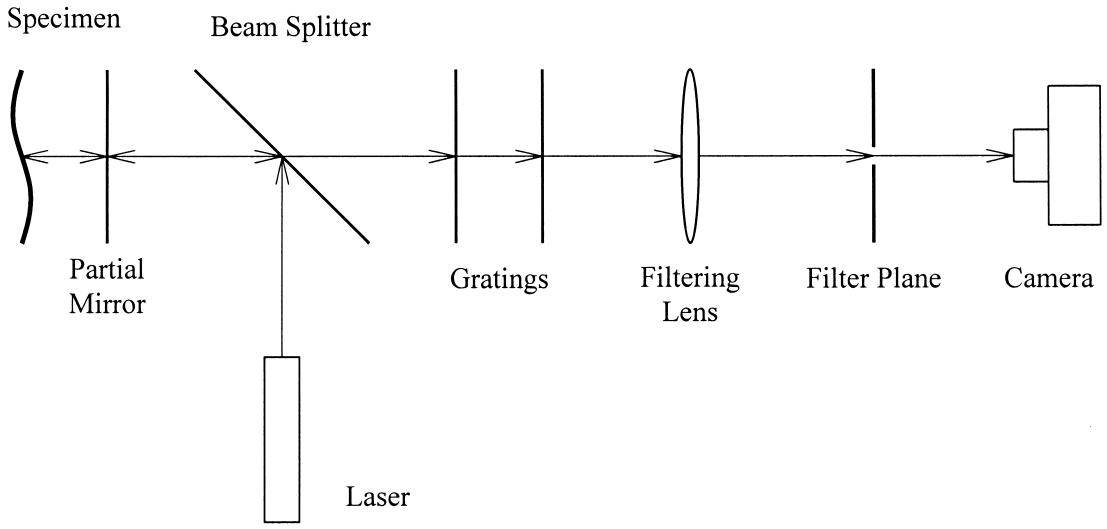

Fig. 7—Schematic of the coherent gradient sensing setup in reflection mode using a partial mirror for fringe multiplication

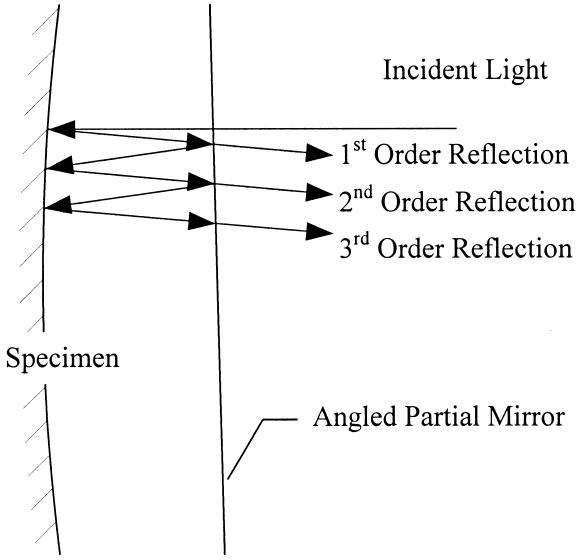

Fig. 8—Light reflection and transmission between the specimen surface and partial mirror

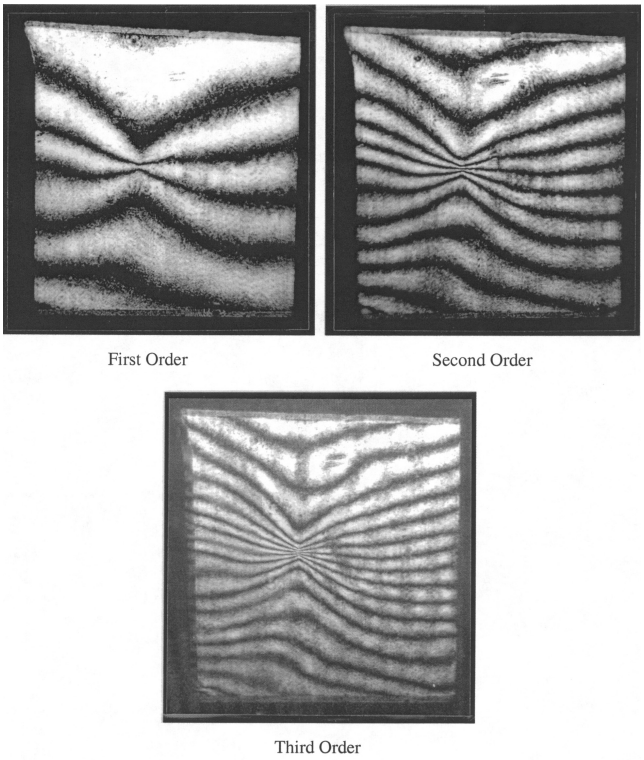

Fig. 9—Fringe multiplication coherent gradient sensing interferograms obtained for a thin film chromium-coated silicon wafer with a localized surface defect

stress to the temperature increase via a relation that involves elastic properties of the film and the substrate as follows:

$$\sigma^f = \frac{E_f/(1-\nu_f)}{\left[\frac{3h}{t}\,\frac{E_f/(1-\nu_f)}{E_s/(1-\nu_s)} - 1\right]}(\alpha_f - \alpha_s)\Delta T, \qquad (12)$$

where σ^f is the film stress, h is the film thickness, t is the substrate thickness, E_f and ν_f are Young's modulus and Poisson's ratio of the film, E_s and ν_s are Young's modulus and Poisson's ratio of the substrate, α_f is the coefficient of thermal expansion of the film, α_s is the coefficient of thermal expansion of the substrate and ΔT is the change in temperature. The deviation of the film stress as obtained from eq (11) from that obtained from the linear elastic case represented by eq (12) will then correspond to cases in which the film is deforming in an inelastic manner. This inelastic deformation represents plastic deformation of the thin film, either in tension or in compression, during the course of the thermal cycle.

For the case in which the film deforms in an elastic manner, one can also relate the normal variation of the stresses in the thin film at a distance x_3 from the film-substrate interface to the curvature component:[30]

$$\sigma^f_{aa}(x_3) = \kappa_{aa} \cdot \frac{E_s}{1-\nu_s}\left\{-\frac{t^3}{6h(h+t)}\left[1+\left(\frac{h}{t}\right)^3\rho\right]+x_3\rho\right\} \quad (13)$$

$$\alpha \in \{1,2\} \quad \text{no sum over } \alpha$$

$$\rho = [E_f/(1-\nu_f)]/[E_s/(1-\nu_s)]. \quad (14)$$

Thermal cycling experiments were conducted on an aluminum film sputtered onto a silicon substrate. Details of the thin film specimen are given in Table 3. The specimen was subjected to a predetermined and controlled thermal cycle. It was heated at a steady rate of 9.4×10^{-2} °C/s from 25°C to 340°C and then cooled back to 25°C at a steady rate of -11.7×10^{-2} °C/s. The slow heating and cooling rates were used to maintain the specimen in thermal equilibrium throughout the experiment. As the specimen was subjected to thermal cycling, the curvature was measured and recorded in real time using CGS. Figure 10 shows a variation of the specimen curvature, κ_{22}, as a function of the specimen temperature. From this variation of specimen curvature, it is possible to determine the stress in the aluminum thin film using eq (11). The variation of stress in the aluminum thin film is plotted in Figure 11. It is evident from the figure that the temperature cycling of the Al-Si specimen resulted in stress cycling of the thin film itself.

At the start of the experiment, the specimen had a nonzero curvature and was in a state of residual tension, which was due to specimen fabrication at an elevated temperature. The aluminum thin film was sputtered onto the silicon substrate at about 200°C. When this specimen was cooled to ambient room temperature, the mismatch in the coefficients of thermal expansion resulted in a state of high residual tension in the film. As the specimen was heated during the experiment, the tensile stresses in the aluminum film decreased linearly as it underwent elastic unloading. The stresses went to zero close to a specimen temperature of 0°C, after which the stresses became compressive. Upon further heating, the compressive stresses increased and the aluminum film yielded in compression. This point was marked by a deviation from linearity in the stress-temperature variation. The compressive stresses continued to increase as the specimen was heated up to 340°C. At this point, the aluminum film was in a state of biaxial compression. As the specimen was cooled, the compressive stresses in the aluminum film decreased linearly as it underwent elastic unloading. The stresses once again become zero around 295°C. Upon further cooling, the film was subjected to elastic loading and acquired increasingly tensile stresses. These stresses caused the film to yield at 240°C when the film stress, σ_{22}, reached a value of 100 MPa. The tensile yield point at 240°C was marked by the deviation from linearity in the stress-temperature variation, as shown in Figure 11. Cooling the specimen further only increased the tensile stress in the aluminum film. As illustrated by this experiment, it is possible to use temperature cycling and curvature measurement to determine the stress-strain behavior and yield properties of thin films deposited on a substrate. In this experiment, the yield stress of the aluminum film at 240°C was determined to be 100 MPa in tension. To determine this, we have assumed that the thin film is plastically isotropic and obeys the Huber–Von Mises yield criterion:

$$\frac{1}{2}S_{ij}S_{ij} = \tau_o^2 = \frac{\sigma^2}{3} \quad \text{where} \quad S_{ij} = \sigma_{ij} - \frac{1}{3}\sigma_{kk}\delta_{ij}. \quad (15)$$

In the above relation, S_{ij} are the Cartesian components of the stress deviator, σ_{ij} are the components of the Cauchy stress tensor, τ_o is the yield stress in shear and $\pm\sigma_o$ are the yield stresses in tension or compression. If one assumes that every point in the film is under a state of pure biaxial tension or compression, that is, if $\sigma^f_{11} = \sigma^f_{22} = \sigma^f$ with all other stresses vanishing, that is, $\sigma_{33} = \sigma_{12} = \sigma_{32} = \sigma_{31} = 0$, then the surviving components of the deviatoric stress are $S_{11} = \sigma^f/3$, $S_{22} = \sigma^f/3$, $S_{33} = 2\sigma^f/3$ and $S_{ij} = 0\ (i \neq j)$ and the yield criterion reduces to

$$\left|\sigma^f\right| = \sigma_o. \quad (16)$$

Equation (16) now implies that under the assumptions stated above, the magnitude of the biaxial stress, σ^f, at the onset of yielding is equal to the yield stress of the material in uniaxial

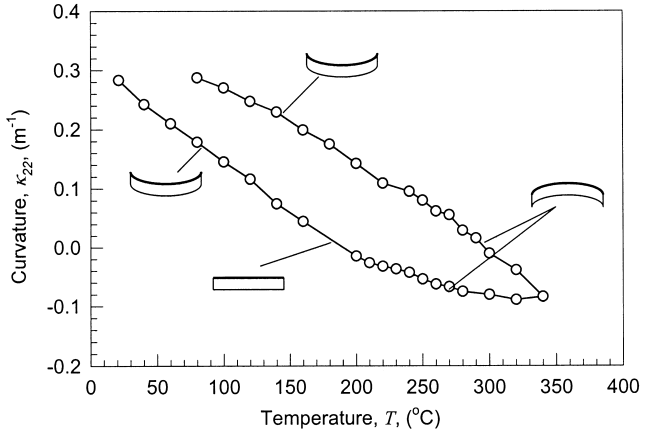

Fig. 10—Variation of specimen curvature as a function of temperature

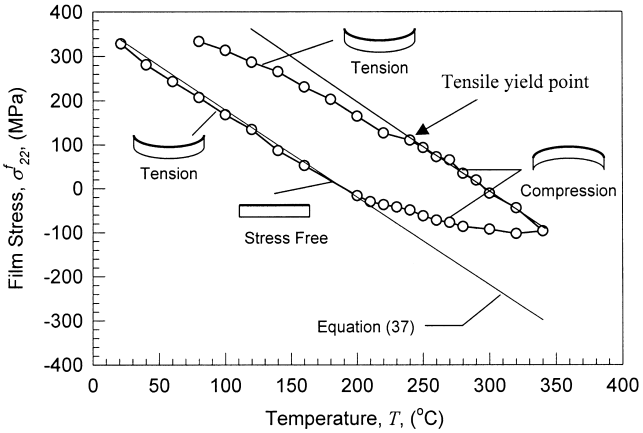

Fig. 11—Variation of thin film stress as a function of the specimen temperature

TABLE 3—DETAILS FOR THE Al-Si SPECIMEN USED IN THE TEMPERATURE-CYCLING EXPERIMENT TO DETERMINE YIELD PROPERTIES OF THE ALUMINUM THIN FILM

Property	Al Thin Film	Si Substrate
Thickness	1.1 μm	200 μm
Young's modulus	75 GPa	130 GPa
Poisson's ratio	0.32	0.32
Coefficient of thermal expansion	23×10^{-6}/°C	3×10^{-6}/°C

tension/compression; that is, $\sigma_{11}^f = \sigma_{22}^f = \sigma^f = \sigma_o$. For the experimental system described above, the yield stress was found to be equal to 100 MPa at 240°C as determined from the deviation of the stress temperature variation from elastic linearity during the purely tensile portion of the thermal cycle.

Summary

This paper presents the full-field optical technique of CGS as a tool for instantaneously measuring curvature tensor fields in thin films. CGS offers several advantages inherent to all full-field optical techniques. It provides real-time, remote, nonintrusive, full-field measurements of curvature. Moreover, because it provides out-of-plane gradients of the specimen surface topography, $x_3 = f(x_1, x_2)$, the technique is insensitive to rigid-body rotation or displacement of the specimen surface. Thus, unlike other interferometric techniques, such as Twyman-Green interferometry,[33,34] CGS is relatively vibration insensitive. In addition, because CGS measures gradients of surface topography, only one differentiation operation of the experimental data is required to obtain curvature. This is in contrast to other traditional interferometric techniques in which curvature calculations involve two successive differentiation operations. Finally, the application of CGS requires only a specularly reflective surface. Unlike X-ray diffraction methods that require the substrate to be a single crystal, CGS is not restricted by the form of the substrate.

To enhance the sensitivity of the CGS technique, we employed the optical method of fringe multiplication by introducing a partial mirror in front of the specimen. The effect of this partial mirror is to reflect light back at the specimen surface. Each such reflection increases the optical path difference introduced in the light beam due to specimen curvature and, thus, enhances the sensitivity of the CGS technique. Because the sensitivity is increased using an optical method, all the advantages of the CGS technique are maintained.

Finally, curvature measurement was employed to determine the stress-strain behavior and yield properties of an aluminum thin film deposited on a silicon substrate. The film was loaded by varying the temperature of the specimen, and the film stress was determined from measurements of specimen curvature. The tensile yield stress of a 1.1-μm aluminum film was determined to be 100 MPa.

Acknowledgments

We would like to acknowledge the financial support through the Jet Propulsion Laboratory's (JPL) Center for Integrated Space Microsystems, System on a Chip program. Many helpful discussions with Dr. E. Kolawa, Dr. S. Kayali and Dr. U. Lieneweg of JPL are also acknowledged.

References

1. International Technology Roadmap for Semiconductors, Semiconductor Industry Association, San Jose, CA (1997).

2. Seidel, T. and Zhao, B., "0.1 μm Interconnect Technology Challenges and the SIA Roadmap," Proceedings of the 1996 MRS Spring Symposium, **427**, *3–16 (1996).*

3. Nix, W.D., "Mechanical-properties of Thin-films," Metallurg. Trans. A, **20**, *2217–2245 (1989).*

4. Li, C.-Y., Totta, P., and Ho, P., eds., Stress Induced Phenomena in Metallization: First International Workshop, AIP Conference Proceedings, **263** *(1992).*

5. Ho, P.S., Li, C.-Y., and Totta, P., eds., Stress Induced Phenomena in Metallization: Second International Workshop, AIP Conference Proceedings, **305** *(1993).*

6. Klema, J., Pyle, R., and Domangue, E., "Reliability Implications of Nitrogen Contamination During Deposition of Sputtered Aluminum/Silicon Metal Films," Proceedings of the 22nd Annual IEEE International Reliability Physics Symposium, 1–5 (1984).

7. Tokunaga, K. and Sugawara, K., "Influence of Plasma Silicon Nitride Passivation Film Quality on Aluminum Void Formation," J. Electrochem. Soc., **138**, *176–180 (1991).*

8. McPherson, J.W. and Dunn, C.F., "A Model for Stress-induced Metal Notching and Voiding in Very Large-scale-integrated Al-Si (1 Percent) Metallization," J. Vacuum Sci. Tech. B, **5**, *1321–1325 (1987).*

9. Yost, F.G., "Voiding Due to Thermal Stress in Narrow Conductor Lines," Scripta Metallurgica et Materialia, **23**, *1323–1328 (1989).*

10. Sauter, A.I. and Nix, W.D., "Study of Stress-driven Diffusive Growth of Voids in Encapsulated Interconnect Lines," J. Mat. Res., **7**, *1133–1143 (1992).*

11. Korhonen, M.A., Paszkiet, C.A., Black, R.D., and Li, C.-Y., "Stress Relaxation of Continuous Film and Narrow Line Metallizations of Aluminum on Silicon Substrates," Scripta Metallurgica et Materialia, **24**, *2297–2302 (1990).*

12. Ryan, J.G., Riendeau, J.B., Shore, S.E., Slusser, G.J., Beyar, D.C., Bouldin, D.P., and Sullivan, T.D., "The Effects of Alloying on Stress-induced Void Formation in Aluminum-based Metallizations," J. Vacuum Sci. Tech. A, **8**, *1474–1479 (1990).*

13. Mayumi, S., Umemoto, T., Shishino, M., Nanatsue, H., Ueda, S., and Inoue, M., "Effect of Cu Addition to Al-Si Interconnects on Stress Induced Open-circuit Failures," Proceedings of the 25th Annual IEEE International Reliability Physics Symposium, 1–5 (1987).

14. Tanikawa, A. and Okabayashi, H., "Observation of Stress-induced Voiding with an Ultra-high Voltage Electron Microscope," Proceedings of the 28th Annual IEEE International Reliability Physics Symposium, 209–215 (1990).

15. Tezaki, A., Mineta, T., and Egawa, H., "Measurement of Three Dimensional Stress and Modeling of Stress Induced Migration Failure in Aluminum Interconnects," Proceedings of the 28th Annual IEEE International Reliability Physics Symposium, 221–229 (1990).

16. Moske, M.A., Ho, P.S., Mikalsen, D.J., Cuomo, J.J., and Rosenberg, R., "Measurement of Thermal-stress and Stress-relaxation in Confined Metal Lines: 1. Stresses During Thermal Cycling," J. Appl. Phys., **74**, *1716–1724 (1993).*

17. Borgesen, P., Korhonen, M.A., and Li, C.-Y., "Stress and Current Induced Voiding in Passivated Metal Lines," Thin Solid Films, **220** *(1-2), 8–13 (1992).*

18. Sanchez, J.E., Jr., Kraft, O., and Arzt, E., "Electromigration Induced Transgranular Slit Failures in Near Bamboo Al and Al-2-percent Cu Thin-film Interconnects," Appl. Phys. Lett., **61**, *3121–3123 (1992).*

19. Blech, I.A., "Stress Effects in Electromigration," J. Electrochem. Soc., **131**, *C325 (1985).*

20. Ho, P.S. and Kwok, T., "Electromigration in Metals," Rep. Prog. Phys., **52**, *301–348 (1989).*

21. Hoang, H.H. and McDavid, J.M., "Electromigration in Multilayer Metallization Systems," Solid State Tech., **30** *(10), 121–126 (1987).*

22. Vaidya, S., Fraser, D.B., and Lindenberger, W.S., "Electromigration in Fine-line Sputter-gun Al," J. Appl. Phys., **51**, *4475–4482 (1980).*

23. Lloyd, J.R., Smith, P.M., and Prokop, G.S., "Role of Metal and Passivation Defects in Electromigration-induced Damage in Thin Film Conductors," Thin Solid Films, **93** *(3-4), 385–395 (1981).*

24. Gardner, D.S., Meindl, J.D., and Saraswat, K.C., "Interconnection and Electromigration Scaling Theory," IEEE Trans. Electronic Devices, **34**, *633–643 (1987).*

25. Danso, K.A. and Tullos, L., "Thin Film Metallization Studies and Device Lifetime Prediction Using Al-Si and Al-Cu-Si Conductor Test Bars," Microelectronics Reliab., **21**, *513–527 (1981).*

26. Cullity, B.D., Elements of X-ray Diffraction, Addison-Wesley, Reading, MA (1978).

27. Tsai, C.-J., Dommann, A., Nicolet, M.-A., and Vreeland, T., "Self-consistent Determination of the Perpendicular Strain Profile of Implanted Si by Analysis of X-ray Rocking Curves," J. Appl. Phys., **69**, *2076–2079 (1991).*

28. Flinn, P.A., Gardner, D.S., and Nix, W.D., "Measurement and Interpretation of Stress in Aluminum-based Metallization as a Function of Thermal History," IEEE Trans. Electronic Devices, **34**, *689–699 (1987).*

29. Stoney, G.G., "The Tension of Metallic Films Deposited by Electrolysis," Proc. Roy. Soc. Lon. Ser. A, **82**, *172 (1909).*

30. Finot, M. and Suresh, S., "Small and Large Deformation of Thick and Thin-film Multi-layers: Effects of Layer Geometry, Plasticity and Compositional Gradients," J. Mech. Phys. Solids, **44**, *683–721 (1996).*

31. Freund, L.B., "Stress Distribution and Curvature of a General Compositionally Graded Semiconductor Layer," J. Crystal Growth, **132**, *341–344 (1993).*

32. Freund, L.B., "Some Elementary Connections Between Curvature and Mismatch Strain in Compositionally Graded Thin Films," J. Mech. Phys. Solids, **44**, *723–736 (1996).*

33. Born, M. and Wolf, E., Principles of Optics, Pergamon Press, New York (1986).

34. Han, B. and Guo, Y., "Thermal Deformation Analysis of Various Electronic Packaging Products by Moire and Microscopic Moire Interferometry," J. Electronic Packaging, **117**, *185–191 (1995).*

35. Rosakis, A.J., Singh, R.P., Tsuji, Y., Kolawa, E., and Moore, N.R., Jr., "Full Field Measurements of Curvature Using Coherent Gradient Sensing: Application to Thin Film Characterization," Thin Solid Films, **325** *(1-2), 42–54 (1998).*

36. Rosakis, A.J., Singh, R.P., Kolawa, E., and Moore, N.R., Jr., "Coherent Gradient Sensing Method and System for Measuring Surface Curvature," U.S. Patent No. 6,031,611 (2000).

37. Lee, Y.J., Lambros, J., and Rosakis, A.J., "Analysis of Coherent Gradient Sensing (CGS) by Fourier Optics," Opt. Lasers Eng., **25** *(1), 25–53 (1996).*